

Microwave Radiometer Radio-Frequency Interference Detection Algorithms: A Comparative Study

Sidharth Misra, Priscilla N. Mohammed, *Member, IEEE*, Bariş Güner, Christopher S. Ruf, *Fellow, IEEE*, Jeffrey R. Piepmeier, *Member, IEEE*, and Joel T. Johnson, *Fellow, IEEE*

Abstract—Two algorithms used in microwave radiometry for radio-frequency interference (RFI) detection and mitigation are the pulse detection algorithm and the kurtosis detection algorithm. The relative performance of the algorithms is compared both analytically and empirically. Their probabilities of false alarm under RFI-free conditions and of detection when RFI is present are examined. The downlink data rate required to implement each algorithm in a spaceborne application is also considered. The kurtosis algorithm is compared to a pulse detection algorithm operating under optimal RFI detection conditions. The performance of both algorithms is also analyzed as a function of varying characteristics of the RFI. The RFI detection probabilities of both algorithms under varying subsampling conditions are compared and validated using data obtained from a field campaign. Implementation details, resource usage, and postprocessing requirements are also addressed for both algorithms.

Index Terms—Detectors, noise measurement, radiometry, radio spectrum management, remote sensing.

I. INTRODUCTION

MICROWAVE radiometry makes use of natural thermal emission by the Earth's surface and atmosphere to remotely sense its properties (e.g., its composition, abundance, roughness, or temperature) [23]–[25]. The microwave portion of the thermal emission spectrum is often best suited for this purpose because of its sensitivity to a particular property of interest or because it suffers less attenuation by the intervening atmosphere between the source of emission and the sensor. Unfortunately, the relative insensitivity of the microwave region to atmospheric effects also makes it an extremely attractive spectral range for wireless communication and for radars. There

has been explosive growth recently in satellite telecommunication, in high-bandwidth point-to-point terrestrial wireless communication links, in wireless routers, and in personal wireless devices like cell phones. Almost all of these users operate in the microwave portion of the spectrum, in or near the bands that are most commonly used for passive microwave remote sensing. As a result, extremely pervasive levels of radio-frequency interference (RFI) have begun to be observed by a number of spaceborne microwave radiometers, particularly in the C- and X-band portions of the spectrum near 6–7 and 10–11 GHz, respectively [1]–[5].

The most blatant instances of RFI manifest themselves as nonphysically bright “hot spots” in images of microwave brightness temperature. Their impact on the measurements can, in some cases, be mitigated if it is possible to isolate them, either temporally or spectrally, from other RFI-free measurements. Such mitigation requires, however, that the presence of the RFI first be detected. Much more prevalent (and insidious) than nonphysical hot spots is low-level RFI that impacts the measurements in similar ways to the expected natural variability in the brightness temperature. Reliable detection of such low-level RFI can be much more difficult. In response to this problem, a number of approaches to low-level RFI detection and mitigation have been developed and implemented recently in both hardware and software. The approaches to detection can be generally divided into four classes: Pulse detection compares the power in samples of the signal (i.e., its second central moment) in the time domain to expected power levels and considers anomalously high values to be caused by RFI [6]. Kurtosis detection evaluates the fourth central moment of a signal divided by the square of its second central moment and considers as RFI those values which differ from that of a Gaussian distributed signal [7]. Cross-frequency techniques examine the power in the signal as function of frequency [8], and spatial methods consider the behavior of brightness temperature as a function of the spatial location [3]. This paper considers only kurtosis and pulse detection algorithms. Both of these algorithms have been implemented and tested in the field with a version of the pulse detection algorithm being applied for the Aquarius mission, and the kurtosis detection algorithm being considered for the upcoming soil moisture active/passive mission.

The pulse detection algorithm can be implemented using either a conventional analog square-law detector or digital signal processing. Kurtosis detection requires specialized detector hardware and/or firmware for implementation [7], [9]. Finer

Manuscript received October 9, 2008; revised April 14, 2009 and August 5, 2009. First published October 16, 2009; current version published October 28, 2009.

S. Misra and C. S. Ruf are with the Space Physics Research Laboratory, Department of Atmospheric, Oceanic and Space Sciences, University of Michigan, Ann Arbor, MI 48109 USA (e-mail: cruf@umich.edu).

P. N. Mohammed is with the Microwave Instrument Technology Branch, NASA Goddard Space Flight Center, Greenbelt, MD 20771 USA, and also with the Goddard Earth Sciences and Technology Center, University of Maryland Baltimore County, Baltimore, MD 21250 USA.

B. Güner is with Halliburton Energy Services, Houston, TX 77032 USA.

J. R. Piepmeier is with the Microwave Instrument Technology Branch, NASA Goddard Space Flight Center, Greenbelt, MD 20771 USA.

J. T. Johnson is with the ElectroScience Laboratory, Department of Electrical and Computer Engineering, The Ohio State University, Columbus, OH 43210 USA.

Color versions of one or more of the figures in this paper are available online at <http://ieeexplore.ieee.org>.

Digital Object Identifier 10.1109/TGRS.2009.2031104

temporal or spectral resolution can be utilized to effectively detect and mitigate RFI. Based on the analog-to-digital (A/D) sampling frequency, a large number of samples are accumulated to give a single radiometer integration sample. If the sampling frequency is higher than the required rate, then the radiometer integration sample can be divided into smaller temporal subsamples giving a better resolution. A temporal subsample accumulates fewer discrete samples than are used for the full integration sample. Thus, RFI mitigation can be accomplished by dividing an integration sample into temporal subsamples and removing only the contaminated ones, by dividing an integration sample into spectral subsamples and removing only the contaminated ones, or a combination of both. In general, any of these mitigation approaches can be used with either of the two approaches to detection [7]–[11].

RFI is often localized in time and/or frequency, relative to the integration times and predetection bandwidths over which a spaceborne microwave radiometer acquires its samples of brightness temperature. As a result, the number of subsamples—in both time and frequency—into which an integration sample is divided can affect the detectability of the RFI. In general, the more closely matched the subsample time and frequency intervals are to the characteristics of the RFI, the better the detection and mitigation. However, such matching requires knowledge of the RFI characteristics and can also often require fairly finely resolved subsamples. Finely resolved temporal subsamples can drive up the data rate of a radiometer. Pulse detection and mitigation implemented in an onboard processor has been demonstrated using terrestrial and airborne radiometers [8], so that increases in data rate may be avoidable. Finely resolved spectral samples can increase both the data rate and the real-time signal processing requirements. The work presented here addresses the cost/benefit tradeoff between the data bandwidth and the quality of RFI detection and mitigation performance as a function of the detection algorithm. The performance of the detection algorithm is assessed with respect to varying RFI parameters both analytically as well as empirically from field data.

In Section II, we give details for both the kurtosis detection algorithm and the pulse detection algorithm. The performance of the two detection algorithms is compared under varying conditions, and relevant results are presented in Section III. Section IV presents an empirical verification of the conclusions obtained from the previous section. Section IV also includes a detailed comparison of the pulse and kurtosis detection algorithms for varying RFI signals obtained during the field campaign. Concluding remarks are given in Section V.

II. RFI DETECTION SYSTEMS

Three separate types of RFI detection systems have been implemented and field tested by the University of Michigan (UM), The Ohio State University (OSU), and the NASA Goddard Space Flight Center (GSFC). The two systems that implement the kurtosis detection algorithm are the UM agile digital detector (ADD) capable of measuring the kurtosis in both temporal and spectral subsamples [7] and the GSFC analog double detector (DD) that measures full-band kurtosis at much finer temporal resolutions [9]. The third system, the OSU

L-band interference suppression radiometer (LISR), includes both a 0.1-MHz spectral resolution as well as a real-time pulse detection and mitigation algorithm [6].

A. Kurtosis Detection Algorithm

Natural thermal emission incident on a spaceborne radiometer and the thermal noise generated by the receiver hardware itself are both random in nature. The kurtosis algorithm makes use of the randomness of the incoming signal to detect RFI. Thermally generated radiometric sources have an amplitude probability distribution function that is Gaussian in nature, whereas man-made RFI sources tend to have a non-Gaussian distribution [7]. The kurtosis algorithm measures the deviation from normality of the incoming radiometric source to detect the presence of interfering sources.

The kurtosis detection algorithm measures higher order central moments of the incoming signal than the second central moment measured by a square-law detector in a total power radiometer. The n th central moment of a signal is given by

$$m_n = \langle (x(t) - \langle x(t) \rangle)^n \rangle \quad (1)$$

where $x(t)$ is the predetection voltage and $\langle \cdot \rangle$ represents the expectation of the measured signal. The kurtosis is the ratio of the fourth central moment to the square of the second central moment, or

$$\kappa = \frac{m_4}{m_2^2} \quad (2)$$

The kurtosis equals three when the incoming signal is purely Gaussian distributed, and it, in most cases, deviates from three if there is a non-normal (typically man-made) interfering source present. The kurtosis statistic is independent of the second central moment of the signal, i.e., the kurtosis value is not affected by natural variations in the brightness temperature of the scene being observed.

The kurtosis estimate itself behaves like a random variable since it is generally calculated from a finite sample set [12]. Estimates of the kurtosis have a standard deviation associated with them, and there is a corresponding kurtosis threshold for detecting RFI. If the sample size is sufficiently large, the kurtosis estimate exhibits a normal distribution.

1) *ADD*: The kurtosis detection algorithm is implemented using the ADD. The ADD is capable of performing standard functions of a conventional analog detector as well as measuring higher order statistics for removal of low-level RFI [7].

ADD's basic design consists of an A/D converter (ADC) followed by 8 to 16 subband digital FIR filters implemented on a field-programmable gate array. These filters provide spectral subsampling of the incoming signal. The output signals from the filters are then accumulated over a temporal subsampling period to measure either the probability distribution function of the signal or its first four noncentral moments.

Due to digitization effects such as rounding, truncating, quantization bin size, ADC span, etc., the expected value of the kurtosis is shifted slightly, but these effects can be corrected for in postprocessing [13]. The simulation results used in the algorithm comparisons presented in Section III assume no

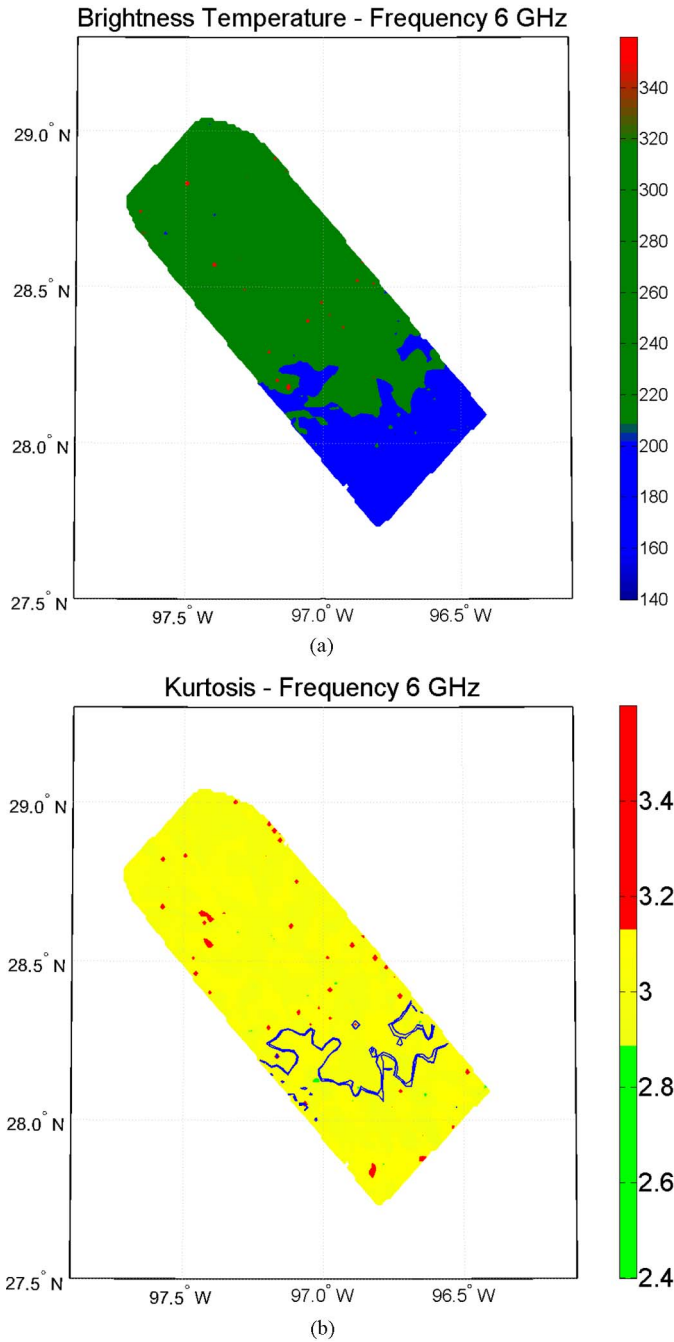


Fig. 1. Images of 6.0-GHz horizontally polarized (a) brightness temperature and (b) kurtosis during an overpass of the Gulf coast near Galveston, TX. The bottom plot of kurtosis has a blue coastal map added over it showing the insensitivity of kurtosis to brightness temperature changes.

quantization effects. ADD has been deployed in many field campaigns, with successful results [7], [14], [15].

Fig. 1 shows RFI detection using the kurtosis statistic obtained from ADD installed in parallel with the standard back-end detector subsystem of the stepped-local oscillator C-band channel of the National Oceanic and Atmospheric Administration/Environmental Technology Laboratory Polarimetric Scanning Radiometer (PSR). PSR employed a frequency scanning technique that covered a range of approximately 5.5–7.7 GHz with a channel resolution of 100 MHz. The figure represents data over the Gulf of Mexico measured at

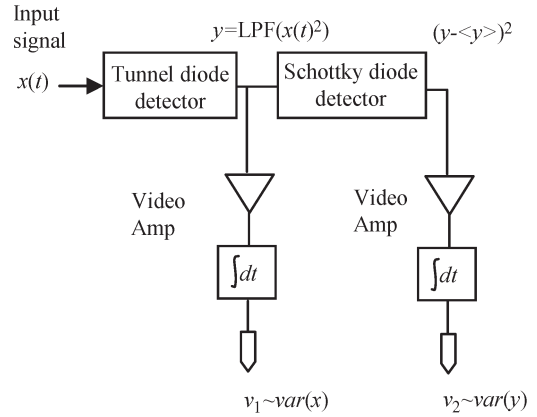


Fig. 2. Block diagram of DD system.

approximately 6.0 GHz. The transition at the coastline from land to water is evident in the brightness temperature image [Fig. 1(a)] because of the high contrast in their emissivities. Discrete “hot spots” in the brightness temperature image are likely a result of RFI sources on the ground. The value of the kurtosis for natural thermal emission is approximately three and does not change with brightness temperature. For example, the transition from high land to low water brightness temperature has no effect whatsoever on the kurtosis image [Fig. 1(b)]. The kurtosis of non-thermal RFI sources, on the other hand, is markedly different and stands out prominently in the image. Assuming a pulsed-sinusoidal type of RFI, kurtosis higher than three represents RFI with a duty cycle less than 50% and kurtosis less than three represents RFI with a duty cycle more than 50%. The duty cycle is measured relative to the radiometer integration period.

2) *NASA Analog Kurtosis DD*: The DD also measures the kurtosis statistic for use in non-Gaussian RFI detection. The system includes a tunnel diode detector which measures the second central moment of the incoming signal $x(t)$ followed by a Schottky diode detector whose output includes the fourth central moment of $x(t)$ (see Fig. 2). The two output voltages are used to approximate the kurtosis. This approximation is referred to as the pseudokurtosis or ψ .

The pseudokurtosis measurement using the DD behaves similarly to the true kurtosis and is defined as

$$\psi \equiv \frac{\text{var}(y)}{\langle y \rangle^2} \tag{3}$$

where $y(t)$ is the baseband video signal [low-pass filtered $x^2(t)$ or $\text{LPF}(x^2(t))$] of the detected RF $x(t)$ and the operators var and $\langle \cdot \rangle$ denote the variance and the expected value, respectively. If $x(t)$ is a band-limited Gaussian random process (which is the case when RFI is absent) then $y(t)$ is exponentially distributed. For exponential distributions $\text{var}(y) = \langle y \rangle^2$ thus ψ reduces to one instead of three. Diode detectors are inherently nonlinear; therefore, in order to use ψ to detect RFI, higher order nonlinearities must be characterized and removed (see [9] for a more detailed description of the DD system and the linearization process). The standard deviation of ψ , which determines the RFI detection threshold, has been derived in [12]. The DD system also detects and records power (second moment)

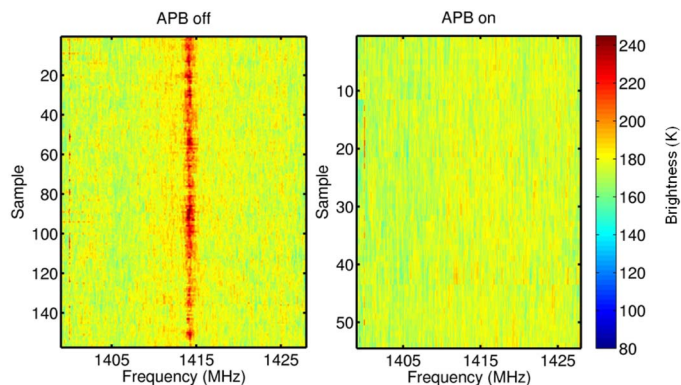


Fig. 3. Spectrograms of calibrated brightness temperatures with and without the APB using data from a campaign in Canton, MI.

measurements with a 2- μ s sampling period so pulse detection (similar to below) can be performed in postprocessing.

B. OSU LISR

In addition to producing spectrograms of received power at 0.1-MHz spectral resolution, LISR includes a real-time pulse detection and mitigation algorithm, called the asynchronous pulse blanker (APB). The APB has been demonstrated to be an effective tool against pulsed RFI [6], [8], [16], [17]. The APB maintains running estimates of the mean and standard deviation of the incoming power which are used to compute a detection threshold. Whenever an integration sample exceeds this threshold, the APB sets to zero a block of such samples beginning from a certain period before the triggering sample, through and hopefully including any multipath components associated with the detected pulses. This operation is completed in an onboard processor in order to avoid increasing the system data rate; calibration effects are corrected by storing the number of blanked samples in a given integration period.

An example illustrating APB performance for pulsed sources is shown in Fig. 3. This figure shows calibrated brightness spectrograms when the APB is turned off (left) and on (right). Horizontal axes in the figures correspond to frequency while the vertical axes are sample indices, proportional to the observation time. These data were obtained from a ground-based campaign in Canton, MI, close to an air route surveillance radar (ARSR) operating at 1315 MHz [10], [17], [21]. The radar observed was reported to have a pulse repetition frequency of 360 Hz and a pulsewidth of 2 μ s. The APB in this campaign operated with a resolution of 10 ns, but the data are integrated onboard so that each output sample corresponds to approximately 269 ms of integration time. A strong RFI corruption at 1415 MHz caused by the aliasing of the radar into the radiometer’s passband is visible in the spectrogram when the APB is off. This source is greatly reduced when the APB is turned on. Another RFI source around 1400 MHz can also be seen in the figures. This source seems to be more continuous in nature so it is less effectively removed by the APB. This example demonstrates the capability of the APB to mitigate pulsed RFI sources in real time without affecting the data rate of a system.

To study the performance of the pulse detector theoretically, an algorithm slightly different from that used in the APB system is considered here. It is based on summing the square

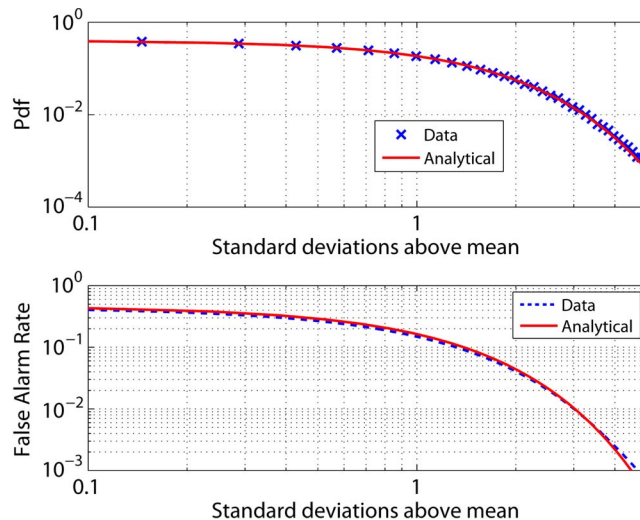


Fig. 4. Comparison of theoretical and experimental (upper) probability density function and (lower) FARs for the pulse detection algorithm test statistic.

of time domain measured fields over N samples. It is assumed that when RFI is absent, successive samples are independent realizations of a zero-mean Gaussian random variable. Given interest in resolving observed fields at varying temporal and spectral resolutions, a radiometer integration period of Q total samples is represented as a set of R subsampling periods of N samples each, so that $Q = NR$. Each of these R sums is a scaled chi-squared random variable with N degrees of freedom when RFI is absent, and is a scaled noncentral chi-squared variable if the N sample integration includes RFI. In the latter case, the noncentrality parameter can be computed if properties of the particular RFI source are specified [18]. The detector selects the maximum of the set of R chi-squared random variables, and compares this maximum to a threshold value. Detection is declared if the threshold is exceeded.

For the RFI-free case, the detection statistic is the maximum of a set of R -scaled chi-squared random variables, for which the probability density function can be determined [18]. This allows the relationship between the threshold value and the false alarm rate (FAR) of the detector to be specified, although doing so requires a good *a priori* estimate of radiometer system temperature (T_{sys}) to be available to set the threshold. The impact of imperfect *a priori* estimations depends strongly on the time resolution of interest, with detectors at shorter time resolutions being less affected. In Fig. 4, analytical and experimental results for the probability density function (upper figure) and the complement of the cumulative distribution function (lower figure) of the pulse detector statistic in an RFI-free case (i.e., the FAR) are compared. The sampling period used in the experimental results is 10 ns, N is 64 samples and there are 416 subsampling periods such that Q is 26 624 samples. For this high time resolution, an excellent match between theory and experiment is obtained; small differences are likely due to the fact that the LISR system was sampling at higher than the Nyquist rate in this experiment, so that successive samples were not completely independent, as assumed in the model. The following discussions consider Nyquist sampling only.

The advantage of this detector is its simplicity, allowing it to be implemented onboard the spacecraft using either analog

or digital methods. If a set threshold (and expected FAR) is utilized, the detector output is a 1-b flag that accompanies the data reported for a radiometer integration period. Mitigation of RFI sources can also be accomplished in real time without affecting the data rate, as demonstrated with the APB experimentally. However, in some applications it may be preferred to downlink all the recorded data at the N -sample integration period, i.e., R power outputs are recorded for each radiometer integration period; this operation greatly increases the required data rate for the pulse detector, but also allows pulse mitigation at a higher time resolution (again assuming such mitigation is not performed onboard). This higher data rate pulse detection process, called the “fully downlinked” pulse detection algorithm, is considered in Section III.

III. PERFORMANCE COMPARISON OF RFI DETECTION ALGORITHMS

A. RFI Model and AUC Parameter

In order to characterize and compare the performance of the detection algorithms, the RFI is modeled as a radar-type pulsed sinusoidal signal. Based on this RFI model, detection statistics such as FAR and probability of detection (PD) are used to generate receiver operating characteristics (ROCs) for both detection algorithms. The ROC curves are then used to parameterize the detection performance of the algorithm.

1) *Modeling RFI*: Air-traffic control radars and early warning radars are expected to be sources of RFI at L-band [19]. In order to compare and contrast the performance of the two detection algorithms, a pulsed-sinusoidal signal is considered as the model for the RFI source. The incoming radiometric signal can be written as

$$x[n] = \begin{cases} a[n], & m \leq n \leq M \\ a[n] + A \sin(2\pi f_o n), & \text{otherwise} \end{cases} \quad (4)$$

where a is a normally distributed random variable with mean μ and standard deviation σ [i.e., $a \sim N(\mu, \sigma)$], A is the amplitude of the pulsed-sinusoid signal with frequency f_o , and M is the total radiometer integration period in units of samples. The duty cycle of the sinusoidal pulse is therefore given by $d = m/M$. For simplicity, the frequency f_o is assumed to be uniformly distributed between 0 and $1/2$ where $f_o = 0$ corresponds to a dc signal and $f_o = 1/2$ corresponds to a signal oscillating at the Nyquist rate. The frequency of each individual pulse is kept constant.

The phase of the pulse onset is assumed to be constant at zero. Since the power and duty-cycle characteristics of RFI are not affected by the phase of the signal, a phase of zero is a valid assumption. It is also assumed that the RFI occurs at the start of the radiometer integration period. Thus, RFI pulse arrival is considered to be synchronous with the start of both the pulse and the kurtosis detection subsampling periods. If the pulsewidth of the incoming RFI signal is considerably smaller than the integration period, the duty cycle or power measured would not change even if the pulse is asynchronous with the start of the subsampling period. Thus, the aforementioned assumption is valid for low duty-cycle RFI. At L-band, typical radar signals that would

cause RFI have a pulsewidth of 2–150 μ s with a pulse repetition frequency of approximately 300 Hz [19]. Such signals result in a duty cycle of 0.2% to 15% with a 1-ms radiometer integration period. For high duty-cycle signals, model predictions would be slightly different. The pulsewidth of the RFI is considered to be an integer multiple of the pulse detection subsampling period.

2) *FAR and PD of Detection Algorithms*: The two RFI parameters that vary in the RFI model presented in the previous section are its duty cycle and amplitude (or power). These parameters significantly affect the detection performance. The behavior of both detection algorithms in the presence of pulsed-sinusoidal RFI has been extensively analyzed previously [11], [18]. The kurtosis detection algorithm is extremely sensitive at low duty cycles. When the pulsed-sinusoidal RFI has a 50% duty cycle, the detection algorithm has a blind spot since the kurtosis value is three. This may not seem to be a problem since most radar signals have a very low duty cycle, but can become important when time subsampling is utilized.

For equal thresholds above and below the kurtosis mean, the FAR of the kurtosis detection algorithm is given by [11]

$$Q_\kappa(z) = \left(1 - \operatorname{erf} \left(\frac{z}{\sqrt{2}} \right) \right) \quad (5)$$

where z is the normalized magnitude of the standard deviation of the kurtosis (i.e., the threshold is set at $3 \pm z\sigma_{R0}$, where σ_{R0} is the standard deviation of RFI-free kurtosis), beyond which a sample is flagged as being corrupted by RFI.

In practical implementations of the detection algorithm the incoming signal is divided into temporal subsamples, or spectral subsamples, or both (Section II-A1) before calculating the kurtosis statistic [7]. If any subsample is flagged, then it is discarded. In order to compare the kurtosis algorithm with other detection algorithms, an entire radiometer integration period is assumed to be corrupted by RFI if any single subsample is flagged. Equation (5) can be rewritten to calculate the FAR for detection of the whole temporal/spectral grid of subsamples within the integration period, as given by

$$Q_\kappa^{\text{noRFI}}(z) = 1 - (1 - Q_\kappa(z))^{XR} \quad (6)$$

where z is the normalized standard deviation magnitude of the kurtosis (i.e., the threshold is set at $3 \pm z\sigma_{R0}$, where σ_{R0} is the standard deviation of RFI-free kurtosis), R is the number of temporal subsampling periods within an entire integration period and X is the number of spectral subbands.

To simplify the analysis, pulsed-sinusoidal RFI is assumed to be located fully within a single-frequency channel of the kurtosis algorithm when spectral subbanding is used; this improves detection performance since the RFI signal-to-noise ratio is larger in this channel. Temporal subsampling also improves detection performance since it reduces the interval over which the RFI power is averaged and hence increases the relative RFI power measured. The analysis allows an RFI pulse to be spread over multiple temporal subsamples if the subsampling period is smaller than the RFI pulsewidth. Subsampling and subbanding reduce the number of independent samples used to calculate kurtosis, as a result of which slight skewness is introduced to the normal distribution of the kurtosis statistic. However,

this skewness is not modeled in what follows. The PD for the kurtosis algorithm for a single subsampling period and a single-frequency channel can be calculated if the duty cycle and power of the RFI signal are known. The PD was given by [11] and is repeated here

$$Q_{\kappa}^{\text{pulsed-sin RFI}}(z) = \left(1 \mp \operatorname{erf} \left(\frac{R_{\text{th}} - \bar{R}(S, d)}{\sqrt{2}\sigma_R(S, d)} \right) \right) \quad (7)$$

where S is the relative power of the pulsed-sinusoidal RFI to the thermal signal, d is the duty cycle of the RFI, \bar{R} and σ_R are the mean and standard deviation of kurtosis for a pulsed-sinusoidal RFI with relative power S and duty cycle d given in [11], $R_{\text{th}} = 3 \pm z\sigma_{R0}$ is the kurtosis threshold and σ_{R0} is the standard deviation of RFI-free kurtosis. As previously mentioned, an integration sample is divided into finer temporal and spectral resolution subsamples, thus creating a grid. In order to detect RFI, the kurtosis with the maximum deviation from three within a temporal and spectral subsampling grid is measured. If that particular kurtosis subsample is above $3 + z\sigma_{R0}$, or below $3 - z\sigma_{R0}$, then the grid is considered to be corrupted by RFI, and hence the whole integration sample is flagged as being corrupted by RFI. Thus, the final PD is obtained by taking the maximum kurtosis deviation among the set of frequency and time resolved kurtosis values.

The pulse detection algorithm performs best when the subsample integration time is matched to the pulsewidth of the RFI. The performance degrades as that subsampling time increases relative to the pulsewidth. For time intervals containing RFI pulses, the power in the incoming signal is a noncentral chi-square random variable with the noncentrality parameter determined by the power and duty cycle of the RFI. The PD of the pulse detection algorithm can be calculated using the right-tail cumulative distribution function of a noncentral chi-squared random variable given in [18] with noncentrality parameter

$$\lambda = \sum_{n=m}^{m+d} A^2 \sin^2(2\pi f_o n) \quad (8)$$

where A is the amplitude of the pulsed-sinusoid signal with frequency f_o and d is the pulsewidth of the RFI, determining the duty cycle.

3) *AUC Parameterization*: The ROC of any detection algorithm is a graphical plot of the PD (fraction of true positives) versus the FAR (fraction of false positives). Fig. 5 shows the ROC curves of the kurtosis and pulse detection algorithms for RFI with $M = 240\,000$, $N = 200$, $d = 800$ (a duty cycle of 0.33% relative to the total integration period) and an average power level of 0.5 NE Δ T. In Fig. 5, two versions of the ROC curve for the kurtosis algorithm are shown: one curve represents the full-band kurtosis with no temporal subsampling and the other assumes 16 spectral subbands are available and the data are subsampled at a rate that is a quarter of the total integration period. The third curve indicates the pulse detection algorithm, with the total integration period divided into 1200 subsampling periods. In general, better detection algorithms correspond to an ROC curve that is closer to the upper left corner of the PD versus FAR space.

In order to estimate the relative performance of the detection algorithms under various conditions, the normalized area under

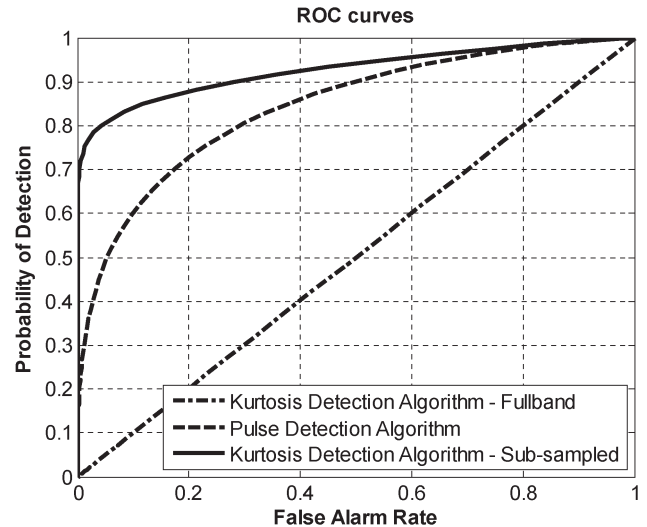


Fig. 5. Plot of the ROC curves for three RFI detection schemes (Pulse-detection algorithm, Full-band kurtosis detection algorithm, Subsampled kurtosis algorithm) for a 0.33% duty-cycle pulsed-sinusoid RFI with a 0.5 NE Δ T power level.

the ROC curve (AUC) is used as a performance metric. An ROC curve that runs diagonally across the PD versus FAR space with a positive slope represents the case of a detector without *a priori* information, i.e., a “50/50” guess as to whether RFI is present or not. The AUC parameter is scaled so that such a case has a performance metric of zero, whereas an AUC of one indicates an ideal detector, with zero probability of false alarms or missed detections. In Fig. 5, the full-band kurtosis algorithm (with a 0.33% duty cycle and 0.5 NE Δ T power level) has an AUC of 0.0012, whereas the subband kurtosis algorithm has an AUC of 0.85 and the pulse detection algorithm has an AUC of 0.69. These values suggest that the subband kurtosis as configured here is the best algorithm for this particular type of RFI. It should be noted that even though one algorithm performs better than the other, the performance might still not be optimal with the current configuration for this type of RFI.

B. Comparison With Pulse Detection Algorithm Under Optimum Resolution

The pulse detection algorithm is considered to be operating under ideal detection conditions when the pulse duration of a pulsed sinusoid RFI is perfectly matched to its subsampling integration time. The performance of the kurtosis algorithm under various spectral and temporal subsampling schemes is compared to such an ideal detector. For comparison, a digital kurtosis detector similar to ADD is considered since subbanding can be easily implemented. An analog kurtosis detector such as DD is equivalent to a full-band digital kurtosis detector with half the data rate. We consider $M = 240\,000$ (for example, a digitizer operating at 240 MHz with a radiometer total integration time of 1 ms), the pulsewidth of RFI is $d = 400$ ($\sim 1.66 \mu\text{s}$ at 240 MHz) for radar signals, and the pulse detection algorithm is nearly optimally matched with $N = 200$ raw samples in one subsample period. The 1.66- μs pulsewidth used in the analysis below is similar to ground-based radars such as the

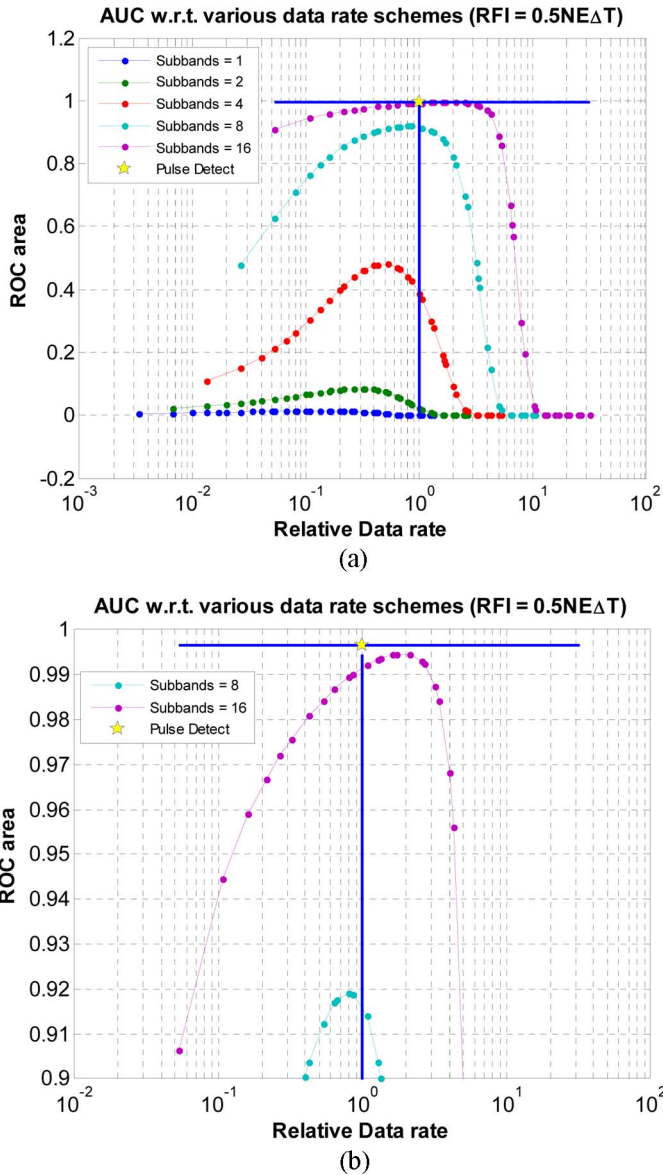


Fig. 6. (a) Plot comparing the ROC area for the kurtosis algorithm as a function of relative data rate and number of subbands with the matched (star) pulse detection algorithm. (b) Magnified plot indicating ROC area of the kurtosis algorithm near matched (star) pulsed detection algorithm (RFI power = 0.5 NEΔT). The relative data rate is with respect to the ideally matched pulse detector.

ARSR-1, 2, and 3. Newer radars such as the ARSR-4 have a typical pulsewidth of 100 μs.

Fig. 6 shows the comparison of the AUC of the kurtosis algorithm with a matched pulse detection algorithm as a function of the relative data rate and the number of subbands. The data rate is an important factor when considering algorithm performance. Even though the pulse detector performs extremely well when matched with the RFI pulsewidth, the resulting data rate (when fully downlinked) due to such finely resolved subsamples for detection and mitigation might be impractical in terms of downlink bandwidth. For RFI mitigation purposes, within a subsampling period, the pulse detection algorithm needs to send only one piece of information, the power (second moment) of the incoming thermal emissions. On the other hand, for a particular temporal subsampling period, the kurtosis detection

algorithm needs to send the first four moments to calculate the kurtosis ratio. These four pieces of information are sent for each subband used by the kurtosis. As a result, for the same temporal period, the kurtosis algorithm has a higher data rate. The data rate for the kurtosis algorithm decreases due to having a much longer subsampling period compared to the pulse detection algorithm. The relative data rate in Fig. 6 is a combined result of these two competing factors (more subbands with four moments versus longer integration period compared to the pulse detection algorithm). The relative data rate can be represented in terms of number of subbands (N), pulse detection subsampling period (τ_p) and kurtosis subsampling period (τ_k) as 4N * τ_p/τ_k.

As shown in Fig. 6, the matched pulse detection algorithm (relative data rate = 1.0) has an almost ideal detection performance (AUC = 1) for an RFI signal with power 0.5 times the NEΔT of the radiometer. The kurtosis detection algorithm with 16 subbands has nearly comparable performance, with an AUC of 0.9 or greater at a significantly lower data rate than the fully downlinked pulse detector. As the subsampling period decreases, the kurtosis detection algorithm performs more poorly, even though the relative RFI to signal power level is higher. This is due to the fact that as the subsampling period becomes shorter, the pulsewidth approaches the 50% duty cycle. At higher RFI power levels, the kurtosis detection algorithm performs nearly as well as the pulse detection algorithm. Fig. 7 is similar to Fig. 6, except that the RFI power is 1.5 times the NEΔT. When using subbanding, there is a larger optimum region of operation of the kurtosis detection algorithm for relatively lower data rates.

C. Algorithm Comparison Under Varying RFI Conditions

Both types of detection algorithm have an optimum operating point in terms of subsample integration time based on certain expected properties of RFI. Considering a typical RFI pulsewidth of d = 400 (1.66 μs), the pulse detection algorithm with subsampling period N = 200 outputs samples at 1200 times the radiometer integration period for assumed sampling conditions. Similarly, based on Section III-B, we find the peak performance for the kurtosis algorithm exists for 16 subbands and a subsampling period that is one-fourth the radiometer integration period. This yields a data rate almost five times lower than the pulse detection algorithm, when compared to storing second moment data at a rate 1200 times the nominal radiometer integration period. If onboard mitigation is implemented or the pulse detector is configured at a slower rate, the data rate reduction becomes less significant.

Even though the detection algorithm parameters are set with respect to expected RFI characteristics, it is necessary to analyze their performance with respect to varying RFI scenarios. Fig. 8 shows the difference in performance between the two detection algorithms in terms of AUC with respect to different RFI power levels and duty cycles. If the AUC for both algorithms is below 0.5, then the detection performance is considered poor enough that the difference can be ignored.

In Fig. 8, a positive value indicates that the kurtosis algorithm performs better and a negative value indicates better pulse detection algorithm performance. The pulse detection

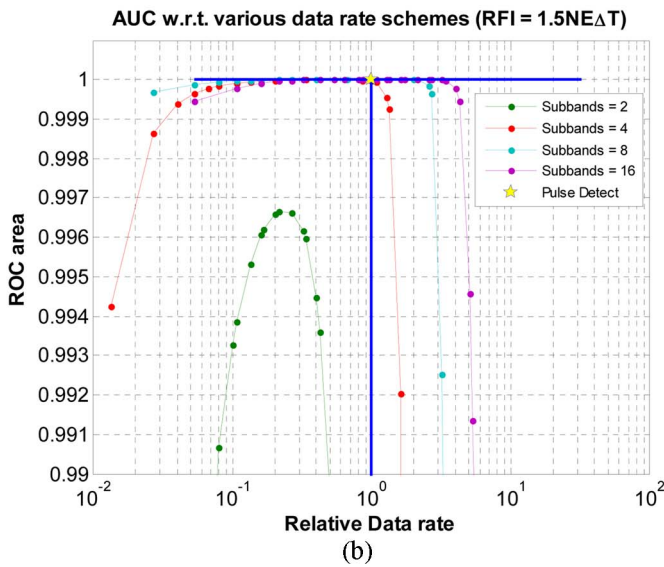
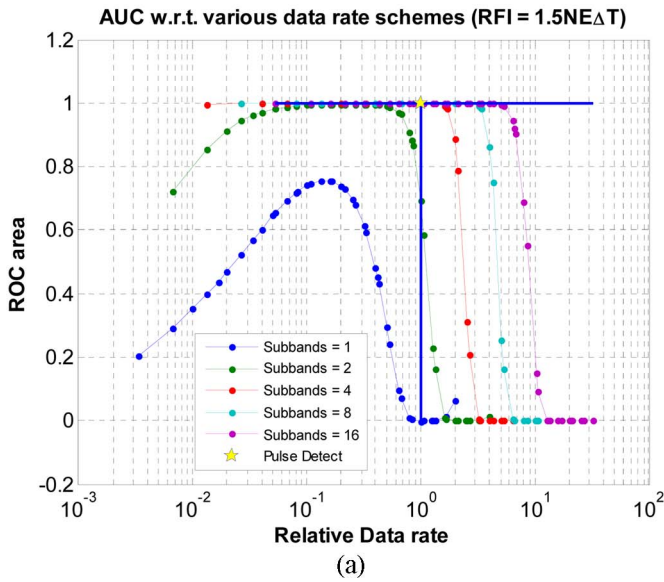


Fig. 7. (a) Plot comparing the ROC area for the kurtosis algorithm as a function of relative data rate and number of subbands with the matched (star) pulse detection algorithm. (b) Magnified plot indicating ROC area of the kurtosis algorithm near matched (star) pulsed detection algorithm (RFI power = 1.5 NE Δ T). The relative data rate is with respect to the ideally matched pulse detector.

algorithm works better when the RFI is optimally matched to its subsampling period, as seen for extremely low duty cycles, although the difference is not large. For low power and low duty cycle, the kurtosis algorithm is more sensitive to RFI whereas for higher duty-cycle signals (continuous-wave) the performance of the pulse detection algorithm degrades significantly as the power decreases. The range of duty cycle of interest for terrestrial radars is approximately 0–0.03 (0%–3%). Within this range the kurtosis detection algorithm shows a significant advantage below 2 NE Δ T RFI magnitude, but no detection advantage over 4 NE Δ T. The kurtosis algorithm with subbanding does however retain a mitigation advantage, particularly at high duty cycles.

Fig. 8 shows a dip around the 0.1–0.15 (10%–15%) duty-cycle region where the performance of the kurtosis algorithm

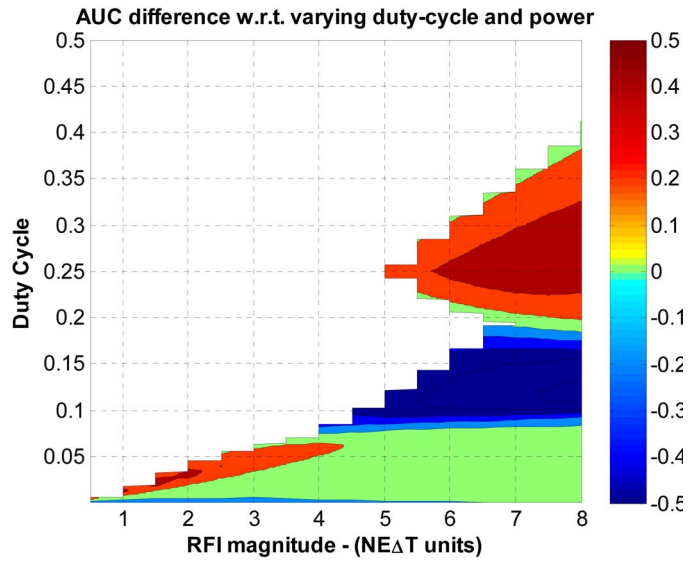


Fig. 8. Plot indicating difference between AUC of the kurtosis detection algorithm and pulse detection algorithm (16 subbands and 4 subsampling periods) for different RFI pulsewidths and duty cycles (Blank areas indicate detection performance of both algorithms is poor, yellow to red areas indicate better performance by the kurtosis detection algorithm, light blue to dark blue areas indicate better performance by the pulse detection algorithm, and green areas indicate similar performance by both algorithms).

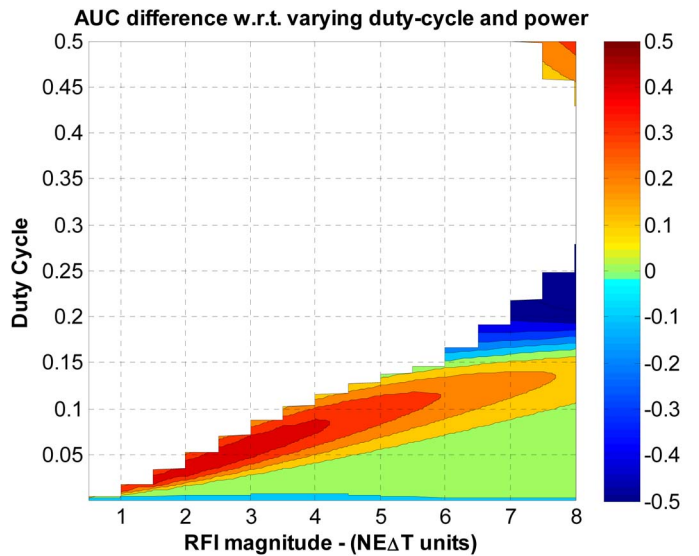


Fig. 9. Plot indicating difference between AUC of the pulse detection algorithm and kurtosis detection algorithm (16 subbands and 2 subsampling periods) for different RFI pulsewidths and duty cycles (Blank areas indicate detection performance of both algorithms is poor, yellow to red areas indicate better performance by the kurtosis detection algorithm, light blue to dark blue areas indicate better performance by the pulse detection algorithm, and green areas indicate similar performance by both algorithms).

degrades significantly. This is due to the fact that the subsampling period approaches the 50% duty cycle of the pulsed-sinusoid RFI. The 50% duty-cycle blind spot can be avoided by combining multiple subsamples in ground postprocessing and recalculating the kurtosis ratio. Thus, the detection performance of the kurtosis algorithm can be improved. Fig. 9 shows the AUC difference when the kurtosis algorithm combines two subsampling periods to a new subsampling period that is half

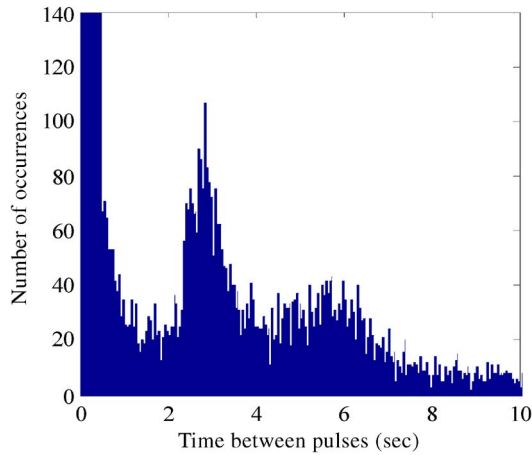


Fig. 10. Data from the night long time series collected on May 10, 2006 to May 11, 2006.

the radiometer integration period. As may be observed in the figure, the blind spot shown in Fig. 8 is easily removed in Fig. 9.

In both of these cases, other algorithms may also become effective for larger duty-cycle pulses, particularly cross-frequency or “peak-picking” approaches. Such algorithms also require an *a priori* estimate of the system brightness temperature, but such estimates are available by excluding the largest brightnesses when computing the mean of the remaining channels. Future work will compare performance with these algorithms; here, the focus is on the pulse and kurtosis algorithms for low duty-cycle pulses.

IV. DETECTION COMPARISON—EXPERIMENTAL VERIFICATION

In this section, an experiment is described whereby the performance of pulse detection is compared to that of the full-band pseudokurtosis-based detector and is examined for its dependence upon radiometer integration time. Experimental data are from a collection made using the DD system interfaced with the passive active L- and S-band (PALS) Radar/Radiometer [22] in 2006 as described in [9]. (In addition, present were the ADD and LISR RFI detection hardware described in Section II.)

A. RFI Environment

Over the course of two weeks, approximately 85 h of data were collected during the Jet Propulsion Laboratories (JPL)/PALS experiment. Many of these data were contaminated with pulse RFI, presumably from near-by airport radars. Because the DD system sampled the radiometer output power at 500 kHz, it proved capable of detecting individual fast radar pulses using a pulse detection algorithm similar to [6]–[20]. The data selected for this experiment were collected on the night of May 10, 2006 to May 11, 2006; over 80 000 pulses were detected during this 18-h period. The distribution of time between pulses is shown in Fig. 10 with a peak evident at 3 s, perhaps the signature of an azimuth sweeping airport radar. Of the detected pulses, 94% of them have pulsewidths of 250 μ s or less and 2% have pulsewidths of 500 μ s or greater.

TABLE I
PULSE STATISTICS FOR DATA ON THE NIGHT OF
MAY 10, 2006 TO MAY 11, 2006

Time Sample	% Pulse Widths $\geq 500 \mu$ s	% Pulse Widths $\leq 250 \mu$ s
18 hours	2	94
7 minutes	9.6	85

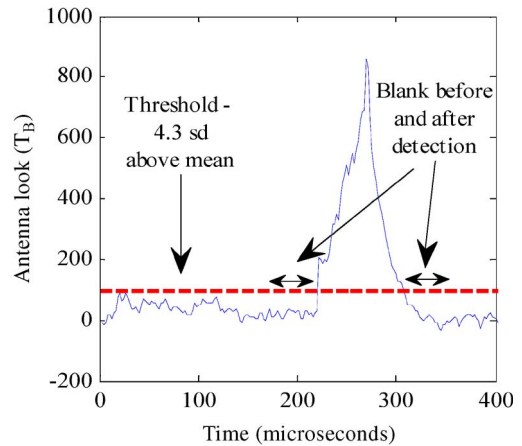


Fig. 11. Fast-sampled (2 μ s) antenna look data at 19:24 PDT on May 10, 2006.

B. Ground Truth Data for Pulse Detection Experiment

A 7-min subset of data, with pulsewidth statistics shown in Table I, was arbitrarily selected for detailed examination. Because most of the cataloged pulses described above were relatively short in time, the RFI-free T_B ground truth was determined using the pulse detection algorithm operating on the native 500-kHz sampled data of the DD system. A pulse detection occurs when

$$T_B(t) - m(t) \geq \beta \sigma(t) \quad (9)$$

where $m(t)$ and $\sigma(t)$ are mean and standard deviation estimates made over 16 ms. (To avoid unduly biasing the estimates with RFI, the largest 10% of samples are removed for the statistic calculation.) The parameter β determines the FAR, which was set to 0.02%, with a β of 4.3. Fig. 11 shows an example of a typical pulse received by PALS that is resolved by the DD fast time series. All samples above the threshold (indicated by the red dashed line) are removed as well as 20 μ s before and after the detected pulse. The remaining samples can be averaged and considered the RFI-free ground truth.

C. Pulse Detection Experiment

The objective of the pulse detection experiment was to evaluate the performance of the pulse blanking algorithm for different integration times. The ground truth data described in the previous section were integrated to create nine RFI-free data sets with integration times ranging from 4 μ s up to 1024 μ s. These data sets are considered ground truth for their respective integration times. The nonmitigated high rate data were integrated to create nine additional data sets of RFI-contaminated data at matching integration times. The pulse blanking algorithm was then applied to the RFI data sets and the results were compared to their ground truths. To keep a constant

TABLE II
THRESHOLD INFORMATION FOR PULSE BLANKING EXPERIMENT

Integration Time (μs)	β
4	4
8	3.9
16	3.8
32	3.7
64	3.65
128	3.6
256	3.6
512	3.57
1024	3.57

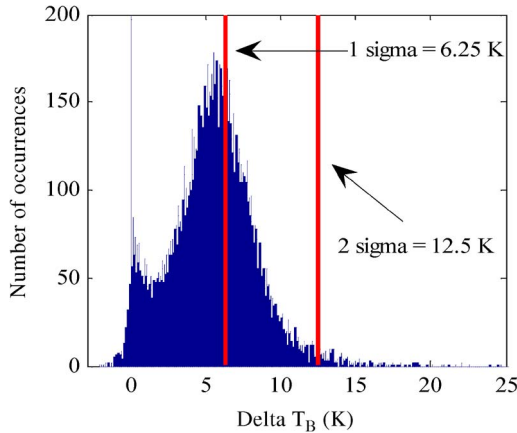


Fig. 12. Pulse blanking experiment—distribution of ΔT_B for 256- μs data.

TABLE III
RESULTS OF PULSE BLANKING AND ψ -DETECTION EXPERIMENTS

Sampling time (μs)	% missed RFI i.e. $\Delta T_B > 0$		% missed RFI with $\Delta T_B > \text{NE}\Delta T$		% missed RFI with $\Delta T_B > 2 \times \text{NE}\Delta T$	
	Pulse	Kurtosis	Pulse	Kurtosis	Pulse	Kurtosis
4	0.0118		0.0342		0	
8	0.125		0.290		0.00645	
16	0.290		4.62		0.122	
32	0.971		32.8		8.13	
64	1.79		50.2		15.5	
128	3.05		52.9		6.44	
256	5.47	5.60	37.3	37.3	1.35	1.60
512		10.3		11.6		0.581
1024		18.9		5.37		0.353
2048		33.8		2.44		0.287
4096		55.8		1.62		0.304
8192		80.34		1.59		0.351
16384		90.03		2.57		0.521

theoretical FAR of 0.02%, the threshold weighting β ranged from 4 to 3.57 depending on the integration time, as shown in Table II.

For each integration time, the ground truth was subtracted from the pulse blanked data and the distribution of this ΔT_B was observed. For example, the distribution of ΔT_B for 256- μs integration time is shown in Fig. 12. Those regions with ΔT_B greater than zero represent missed detections and error in the pulse-blanked brightness temperatures. Distribution statistics for the nine cases are summarized in Table III. The percentage error in T_B greater than 2 $\text{NE}\Delta T$ is used as the measure of performance of the pulse detection algorithm where $\text{NE}\Delta T$ is calculated from the ground truth for each integration time.

The pulse detection algorithm performs quite well for short integration times, but degrades quickly as the integration time

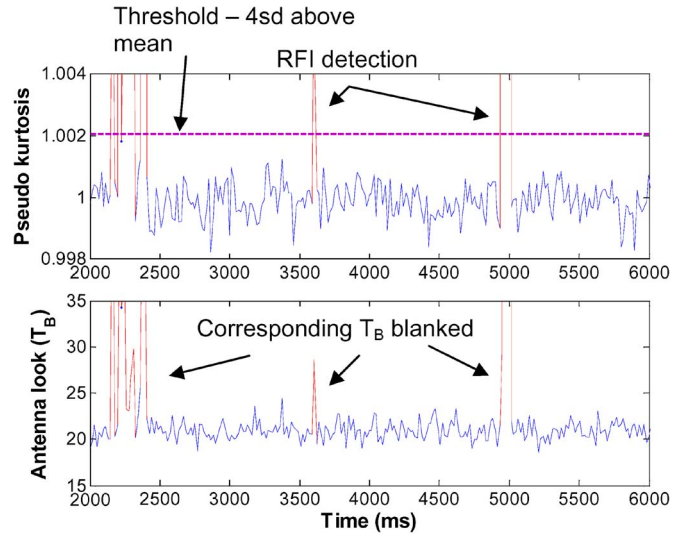


Fig. 13. Sixteen-millisecond data at 19:24 PDT from May 10, 2006 demonstrating ψ detection and blanking.

approaches 64 μs . Improvement is found again as the integration time reaches 256 μs . However, the algorithm fails at an integration time of 512 μs or greater because the mean and standard deviation estimators are inadequate due to a lack of RFI-free samples over a 16-ms window.

D. Pseudokurtosis Detection Experiment

Using the same data as above, pseudokurtosis detection was performed to evaluate its detection capability versus integration time. The 2- μs second and fourth moment data were integrated and ratioed to obtain separate ψ -time series with samples ranging from 256 μs to 16 ms. Shorter integration times were not compared because the kurtosis degraded beyond usability.

A ψ -detection algorithm similar to (9) was used to detect RFI such that RFI detection occurs when

$$|\psi(t) - m(t)| \geq 4\sigma(t) \tag{10}$$

where $m(t)$ and $\sigma(t)$ are the mean and standard deviation of each 14-s time window of ψ data without the outlying 10% of samples. Ideally, the mean and standard deviation of RFI-free ψ data should not vary over time ($\psi \equiv 1$), however, running values were calculated using a small enough time window to account for any thermal drifts in the system. The threshold weighting was set to 4 standard deviations above the mean to give a similar FAR to the pulse detection algorithm. RFI detection and blanking are shown in Fig. 13.

Similarly, statistics for missed RFI ΔT_B (the difference between ψ -blanked T_B and the ground truth) were computed and are presented in Table III. An example ΔT_B histogram is shown in Fig. 14. Although there appear to be a number of missed detections, the majority are by far smaller than $\text{NE}\Delta T$.

E. Results of Pulse Blanking and Pseudokurtosis Detection Experiments

The pulse detection algorithm performs quite well at integration times of 16 μs or less. This is somewhat to be expected since the ground truth was found by mitigating the 2- μs time

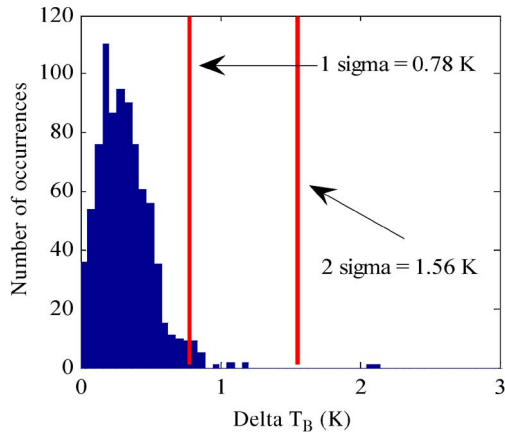


Fig. 14. ψ -detection experiment—distribution of ΔT_B for 16-ms data, ~ 2 min of antenna look data.

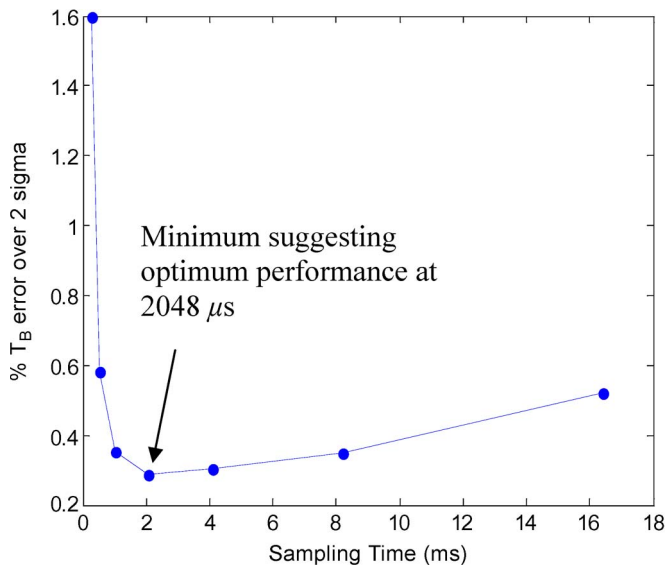


Fig. 15. ψ -kurtosis detection results for varying integration times.

series for pulsed RFI. However, the RFI did exhibit short-pulse characteristics, thus requiring relatively short integration times to approximate matched-filter detection. At integration periods greater than 16 μ s, the pulse detection algorithm did not perform well until reaching 256 μ s, of which only 1.35% of missed detections were larger than $2 \times NE\Delta T$. Similarly, the pseudokurtosis detection algorithm worked reasonably well at the same integration, missing only 1.6% of possible detections greater than $2 \times NE\Delta T$. However, as integration time increased the algorithm performance improved, demonstrating optimal performance at 2048 μ s as shown in Fig. 15. It is likely that the shorter integration times created large duty cycles and longer integration times reduced the interference energy with respect to the thermal noise—both act to reduce detectability.

V. SUMMARY AND DISCUSSION

The pulse detection algorithm and the kurtosis algorithm are two RFI detection techniques developed for microwave remote sensing. The pulse detection algorithm operates on the principle of a simple threshold operation of the radiometric data. This technique requires a high integration rate and short integration

period to optimally identify and mitigate short radarlike RFI pulses. The APB is a system developed by OSU that is an effective tool against RFI. The kurtosis detection algorithm detects RFI based on the Gaussian statistics of the incoming thermal signal. The kurtosis algorithm has been successfully implemented and tested in two different systems: a full-band analog DD developed by GSFC and an ADD developed by UM that uses spectral subbands.

One of the advantages of the pulse detection algorithm is a relatively simple implementation since it needs to measure only power. The digital kurtosis algorithm needs to record the first four moments of the signal, and the implementation can be slightly more complicated if subbanding filters are used as well.

The detectability of both algorithms is characterized using the AUC for pulsed-sinusoid type of RFI signals. Although AUCs give an indication of the detection performance, the final PD and FAR are determined by a single threshold value. Kurtosis is independent of variations in power and hence RFI, and as a result, the threshold value is easily set. The pulse detection algorithm, on the other hand, determines the threshold value based on the incoming data itself. Thus, the threshold might be corruptible by natural brightness temperature variations or worse, RFI, particularly for subsamples that are longer in time. For example, in the APB system of LISR, the onboard estimate of the time-domain power mean and variance is calculated only for samples that are deemed free of RFI. The DD system made estimates by removing large-valued samples, but was shown to break down as the number of available samples became too small.

Results indicate that the pulse detection algorithm has superior detectability when its subsample integration time matches the RFI pulsewidth. If no flagging or onboard mitigation are used, the pulse detection algorithm requires a relatively high integration rate and bandwidth for it to work effectively as an optimal detector and mitigator for very low duty-cycle RFI. However, it provides complementary performance to the kurtosis method in some cases and, if implemented as an onboard flag, can provide useful information without impacting the system data rate. The kurtosis algorithm can achieve nearly the same performance in terms of RFI mitigation at a considerably lower relative data rate, assuming all the subsamples are downlinked in the pulse detection algorithm. Since the pulse detection algorithm works best when the subsampling period is exactly matched to the radar pulsewidth, the algorithm gains no real advantage by recombining the subsamples to improve detection performance, except in the cases where pulsewidths are longer than the subsample period. The kurtosis algorithm with subbanding provides more robust detection when dealing with varying RFI duty cycle and power. The subsampling periods of kurtosis can be combined to remove any blind spots and improve detectability by operating at the optimum accumulation period for a given RFI signal.

The performances of both the algorithms have been empirically compared using data obtained from a field campaign at JPL. GSFC's fast video sampling data are used as ground truth to evaluate the pulse detection algorithm and full-band kurtosis algorithm at separate temporal subsampling periods. Results confirm that for lower subsampling periods, the pulse detection algorithm is better, provided high data bandwidth is available

or mitigation is done onboard. As the subsampling period increases, the kurtosis algorithm performs better with a much lower data rate. However, the kurtosis detection performance degrades when the subsampling period approaches a 50% duty cycle.

REFERENCES

- [1] L. Li, E. G. Njoku, E. Im, P. S. Chang, and K. S. Germain, "A preliminary survey of radio-frequency interference over the U.S. in Aqua AMSR-E data," *IEEE Trans. Geosci. Remote Sens.*, vol. 42, no. 2, pp. 380–390, Feb. 2004.
- [2] E. G. Njoku, T. K. Chan, W. Crosson, and A. Limaye, "Evaluation of the AMSR-E data calibration over land," *Riv. Ital. Telerilev., Italian J. Remote Sens.*, vol. 30, no. 31, pp. 15–33, 2004.
- [3] E. G. Njoku, P. Ashcroft, T. K. Chan, and L. Li, "Global survey and statistics of radio-frequency interference in AMSR-E land observations," *IEEE Trans. Geosci. Remote Sens.*, vol. 43, no. 5, pp. 938–947, May 2005.
- [4] L. Li, P. W. Gaiser, M. H. Bettenhausen, and W. Johnston, "WindSat radio-frequency interference signature and its identification over land and ocean," *IEEE Trans. Geosci. Remote Sens.*, vol. 44, no. 3, pp. 530–539, Mar. 2006.
- [5] S. W. Ellingson and J. T. Johnson, "A polarimetric survey of radio-frequency interference in C- and X-bands in the continental United States using WindSat radiometry," *IEEE Trans. Geosci. Remote Sens.*, vol. 44, no. 3, pp. 540–548, Mar. 2006.
- [6] N. Niamsuwan, J. T. Johnson, and S. W. Ellingson, "Examination of a simple pulse-blanking technique for radio frequency interference mitigation," *Radio Sci.*, vol. 40, no. 5, p. RS5 S03, Jun. 2005.
- [7] C. S. Ruf, S. M. Gross, and S. Misra, "RFI detection and mitigation for microwave radiometry with an Agile Digital Detector," *IEEE Trans. Geosci. Remote Sens.*, vol. 44, no. 3, pp. 694–706, Mar. 2006.
- [8] B. Guner, J. T. Johnson, and N. Niamsuwan, "Time and frequency blanking for radio-frequency interference mitigation in microwave radiometry," *IEEE Trans. Geosci. Remote Sens.*, vol. 45, no. 11, pp. 3672–3679, Nov. 2007.
- [9] J. R. Piepmeier, P. N. Mohammed, and J. J. Knuble, "A double detector for RFI mitigation in microwave radiometers," *IEEE Trans. Geosci. Remote Sens.*, vol. 46, no. 2, pp. 458–465, Feb. 2008.
- [10] C. Ruf and S. Misra, "Detection of radio frequency interference with the aquarius radiometer," in *Proc. IGARSS*, Barcelona, Spain, 2007, pp. 2722–2725.
- [11] R. D. De Roo, S. Misra, and C. S. Ruf, "Sensitivity of the kurtosis statistic as a detector of pulsed sinusoidal RFI," *IEEE Trans. Geosci. Remote Sens.*, vol. 45, no. 7, pp. 1938–1946, Jul. 2008.
- [12] J. F. Kenney and E. S. Keeping, "Kurtosis," in *Mathematics of Statistics*, 3rd ed. Princeton, NJ: Van Nostrand, 1962, ch. 1, pp. 102–103.
- [13] R. D. De Roo and S. Misra, "A demonstration of the effects of digitization on the calculation of kurtosis for the detection of RFI in microwave radiometry," *IEEE Trans. Geosci. Remote Sens.*, vol. 46, no. 10, pp. 3129–3136, Oct. 2008.
- [14] C. Ruf, S. Misra, S. M. Gross, and R. D. De Roo, "Detection of RFI by its amplitude probability distribution," in *Proc. IGARSS*, Denver, CO, 2006, pp. 2289–2291.
- [15] S. Misra and C. S. Ruf, "Detection of radio-frequency interference for the aquarius radiometer," *IEEE Trans. Geosci. Remote Sens.*, vol. 46, no. 10, pp. 3123–3128, Oct. 2008.
- [16] G. A. Hampson, S. W. Ellingson, and J. T. Johnson, "Design and demonstration of an interference suppressing microwave radiometer," in *Proc. IEEE Aerosp. Conf.*, Mar. 2004, vol. 2, pp. 293–299.
- [17] N. Niamsuwan, B. Guner, and J. T. Johnson, "Observations of an ARSR system in Canton, MI with the L-band interference suppressing radiometer," in *Proc. IGARSS*, Denver, CO, 2006, pp. 2285–2288.
- [18] J. T. Johnson and L. C. Potter, "Performance study of algorithms for detecting pulsed sinusoidal interference in microwave radiometry," *IEEE Trans. Geosci. Remote Sens.*, vol. 47, no. 2, pp. 628–636, Feb. 2009.
- [19] J. R. Piepmeier and F. A. Pellerano, "Mitigation of terrestrial radar interference in L-band spaceborne microwave radiometers," in *Proc. IGARSS*, Denver, CO, 2006, pp. 2292–2296.
- [20] S. W. Ellingson and G. A. Hampson, "Mitigation of radar interference in L-band radio astronomy," *Astrophys. J.*, vol. 147, no. 1, pp. 167–176, Jul. 2003.
- [21] J. T. Johnson, B. Guner, and N. Niamsuwan, "Observations of an ARSR System in Canton, MI With the L-Band Interference Suppressing Radiometer," project report, 2005. [Online]. Available: http://esl.eng.ohio-state.edu/~rsttheory/iip/lisr_jtj.pdf
- [22] W. J. Wilson, S. H. Yueh, S. J. Dinardo, S. L. Chazanoff, A. Kitiyakara, F. K. Li, and Y. Rahmat-Samii, "Passive active L- and S-Band (PALS) microwave sensor for ocean salinity and soil moisture measurements," *IEEE Trans. Geosci. Remote Sens.*, vol. 39, no. 5, pp. 1048–1039, May 2001.
- [23] S. H. Yueh, W. J. Wilson, F. Nghiem, and W. Ricketts, "Polarimetric measurements of sea surface brightness temperatures using an aircraft K-band radiometer," *IEEE Trans. Geosci. Remote Sens.*, vol. 33, no. 1, pp. 85–92, Jan. 1995.
- [24] T. J. Schmugge, P. Gloersen, T. Wilheit, and F. Gleiger, "Remote sensing of soil moisture with microwave radiometers," *J. Geophys. Res.*, vol. 79, no. 2, pp. 317–323, 1974.
- [25] A. Stogryn, "The apparent temperature of the sea at microwave frequencies," *IEEE Trans. Antennas Propag.*, vol. AP-15, no. 2, pp. 278–286, Mar. 1967.



Sidharth Misra received the B.E. degree in electronics and communication engineering from the Nirma Institute of Technology, Gujarat University, Ahmedabad, Gujarat, India, in 2004 and the M.S. degree in electrical engineering and computer science—signal processing from the University of Michigan, Ann Arbor, in 2006, where he is currently working toward the Ph.D. degree in the Department of Atmospheric, Oceanic and Space Sciences.

He was a Research Engineer with the Space Physics Research Laboratory, University of Michigan, where he worked on the analysis and implementation of the agile digital receiver for radio-frequency interference (RFI) mitigation. He was also on Oceansat-II with the Space Applications Center, Indian Space Research Organization, Ahmedabad. He was a Research Assistant with the Danish National Space Center, Technical University of Denmark (DTU), Lyngby, Denmark, performing RFI analysis for CoSMOS, which is an airborne campaign preparing for SMOS at DTU. His research interests involve microwave radiometry, signal detection and estimation, and image processing.

Mr. Misra is the recipient of the 2006 International Geoscience and Remote Sensing Symposium (IGARSS) Prize Paper Award and first prize at the IGARSS 2009 Student Prize Paper Competition.



Priscilla N. Mohammed (S'02–M'06) received the B.S. degree in electrical engineering from the Florida Institute of Technology, Melbourne, in 1999 and the M.S. and Ph.D. degrees in electrical engineering from the Georgia Institute of Technology, Atlanta, in 2001 and 2005, respectively.

As a Ph.D. student, she performed microwave measurements of gaseous phosphine and ammonia under simulated conditions for the outer planets and used these measurements to develop a radio occultation simulator to predict absorption and excess

Doppler due to Saturn's atmosphere. Much of this work was in support of the Cassini mission to Saturn. Based on these laboratory results, the Cassini Project Science Group made the decision to extend the Ka-band (32 GHz) operation throughout the mission tour. The predicted attenuation profiles for the Cassini radio occultation maneuver of May 2005 earned her an invitation from the Cassini Radio Science Team to present a paper on their behalf at the 37th Annual Meeting of the Division for Planetary Sciences in Cambridge, U.K. In 2006, she joined the Goddard Earth Sciences and Technology Center, University of Maryland Baltimore County, Baltimore, as a member of the research faculty. She is also with the Microwave Instrument Technology Branch, NASA Goddard Space Flight Center, Greenbelt, MD. Her current research interests include radio-frequency interference mitigation in microwave radiometers.

Barış Güner received the B.S. and M.S. degrees in electrical and electronics engineering from Bilkent University, Ankara, Turkey, in 2002 and 2004, respectively, and the Ph.D. degree in electrical and computer engineering from The Ohio State University, Columbus, in 2009.

He is currently working for Halliburton Energy Services, Houston, TX. His research interests include magnetic resonance imaging, microwave remote sensing, and computational electromagnetics.



Christopher S. Ruf (S'85–M'87–SM'92–F'01) received the B.A. degree in physics from Reed College, Portland, OR, and the Ph.D. degree in electrical and computer engineering from the University of Massachusetts, Amherst.

He was with Intel Corporation, Hughes Space and Communication, the NASA Jet Propulsion Laboratory, and Penn State University, University Park. In 2000, he was a Guest Professor with the Technical University of Denmark, Lyngby, Denmark. He has published in the areas of microwave radiometer satellite calibration, sensor and technology development, and atmospheric, oceanic, land surface and cryosphere geophysical retrieval algorithms. He is currently a Professor of atmospheric, oceanic, and space sciences; a Professor of electrical engineering and computer science; and the Director of the Space Physics Research Laboratory, University of Michigan, Ann Arbor.

Dr. Ruf is a member of the American Geophysical Union (AGU), the American Meteorological Society (AMS), and Commission F of the Union Radio Scientifique Internationale. He has served on the editorial boards of the AGU *Radio Science*, the IEEE TRANSACTIONS ON GEOSCIENCE AND REMOTE SENSING (TGRS), and the AMS *Journal of Atmospheric and Oceanic Technology*. He is currently the Editor-in-Chief of TGRS. He has been the recipient of three NASA Certificates of Recognition and four NASA Group Achievement Awards, as well as the 1997 TGRS Prize Paper Award, the 1999 IEEE Resnik Technical Field Award, and the 2006 International Geoscience and Remote Sensing Symposium Prize Paper Award.

Dr. Ruf is a member of the American Geophysical Union (AGU), the American Meteorological Society (AMS), and Commission F of the Union Radio Scientifique Internationale. He has served on the editorial boards of the AGU *Radio Science*, the IEEE TRANSACTIONS ON GEOSCIENCE AND REMOTE SENSING (TGRS), and the AMS *Journal of Atmospheric and Oceanic Technology*. He is currently the Editor-in-Chief of TGRS. He has been the recipient of three NASA Certificates of Recognition and four NASA Group Achievement Awards, as well as the 1997 TGRS Prize Paper Award, the 1999 IEEE Resnik Technical Field Award, and the 2006 International Geoscience and Remote Sensing Symposium Prize Paper Award.



Jeffrey R. Piepmeier (S'93–M'99) received the B.S. degree in engineering from LeTourneau University, Longview, TX, in 1993 and the M.S. and Ph.D. degrees in electrical engineering from the Georgia Institute of Technology, Atlanta, in 1999 and 1994, respectively.

From 1993 to 1994, he was a Schakleford Fellow with the Georgia Tech Research Institute. In 1999, he joined the Microwave Instrument Technology Branch, NASA Goddard Space Flight Center, Greenbelt, MD, as a Principal Investigator on several

technology development projects in microwave radiometry. During 2004–2005, he led the Hydros radiometer team. He is currently the Calibration Lead for the NASA Aquarius radiometer and Instrument Scientist for the NASA SMAP radiometer.

Dr. Piepmeier is a member of the Union Radio Scientifique Internationale Commission F and the American Geophysical Union. He is a past Chair of the IEEE Geoscience and Remote Sensing Society Instrumentation and Future Technologies technical subcommittee and a 2002 NASA Earth Science New Investigator. He is currently Chair of the National Academies' Committee on Radio Frequencies. He received the third place award in the 1998 International Geoscience and Remote Sensing Symposium Student Prize Paper Competition. He was a recipient of an Excellence in Federal Career Gold Award (Rookie of the Year) in 2000. He was a Chair of the 2000 Microwave Radiometer Calibration Workshop (MicroCal2000). He was the recipient of the NASA Goddard Space Flight Center Exceptional Achievement Award and Technology Advancement Award in 2005 and 2007, respectively.

Joel T. Johnson (S'88–M'96–SM'03–F'09) received the B.S. degree in electrical engineering from the Georgia Institute of Technology, Atlanta, in 1991 and the M.S. and Ph.D. degrees from the Massachusetts Institute of Technology, Cambridge, in 1993 and 1996, respectively.

He is currently a Professor with the ElectroScience Laboratory, Department of Electrical and Computer Engineering, The Ohio State University. His research interests are in the areas of microwave remote sensing, propagation, and electromagnetic wave theory.

Dr. Johnson is a member of Commissions B and F of the International Union of Radio Science (URSI). He was the recipient of the 1993 Best Paper Award from the IEEE Geoscience and Remote Sensing Society, was named an Office of Naval Research Young Investigator, National Science Foundation Career awardee, and the Presidential Early Career Award for Scientists and Engineers award recipient in 1997, and was recognized by the U.S. National Committee of URSI as a Booker Fellow in 2002. He is also a member of Tau Beta Pi, Eta Kappa Nu, and Phi Kappa Phi.